

www.acsami.org Research Article

One-Step Supramolecular Multifunctional Coating on Plant Virus Nanoparticles for Bioimaging and Therapeutic Applications

Zhuohong Wu, Jiajing Zhou, Christian Isalomboto Nkanga, Zhicheng Jin, Tengyu He, Raina M. Borum, Wonjun Yim, Jingcheng Zhou, Yong Cheng, Ming Xu, Nicole F. Steinmetz,* and Jesse V. Jokerst*



Cite This: ACS Appl. Mater. Interfaces 2022, 14, 13692–13702



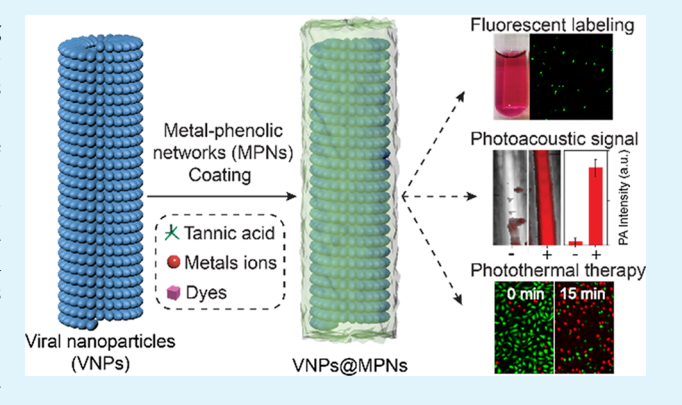
ACCESS

Metrics & More

Article Recommendations

s Supporting Information

ABSTRACT: Plant viral nanoparticles (plant VNPs) are promising biogenetic nanosystems for the delivery of therapeutic, immunotherapeutic, and diagnostic agents. The production of plant VNPs is simple and highly scalable through molecular farming in plants. Some of the important advances in VNP nanotechnology include genetic modification, disassembly/reassembly, and bioconjugation. Although effective, these methods often involve complex and time-consuming multi-step protocols. Here, we report a simple and versatile supramolecular coating strategy for designing functional plant VNPs via metal—phenolic networks (MPNs). Specifically, this method gives plant viruses [e.g., tobacco mosaic virus (TMV), cowpea mosaic virus, and potato virus X] additional functionalities including photothermal transduction, photoacoustic imaging, and fluorescent labeling via different components in MPN coating [i.e.,



complexes of tannic acid (TA), metal ions (e.g., Fe³⁺, Zr⁴⁺, or Gd³⁺), or fluorescent dyes (e.g., rhodamine 6G and thiazole orange)]. For example, using TMV as a viral substrate by choosing Zr⁴⁺–TA and rhodamine 6G, fluorescence is observed peaking at 555 nm; by choosing Fe³⁺–TA coating, the photothermal conversion efficiency was increased from 0.8 to 33.2%, and the photoacoustic performance was significantly improved with a limit of detection of 17.7 μ g mL⁻¹. We further confirmed that TMV@Fe³⁺–TA nanohybrids show good cytocompatibility and excellent cell-killing performance in photothermal therapy with 808 nm irradiation. These findings not only prove the practical benefits of this supramolecular coating for designing multifunctional and biocompatible plant VNPs but also bode well for using such materials in a variety of plant virus-based theranostic applications.

KEYWORDS: metal-phenolic network, plant virus nanoparticles, photothermal therapy, photoacoustic imaging, fluorescent imaging, theranostics

1. INTRODUCTION

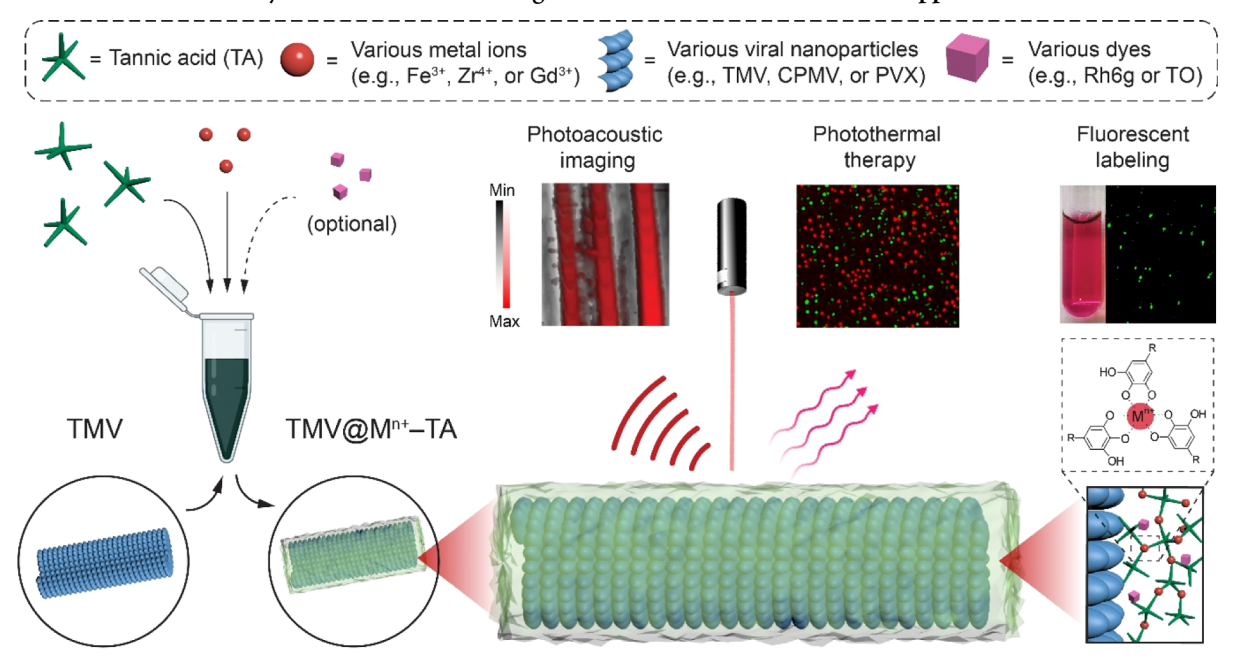
Plant virus nanoparticles (plant VNPs) have attracted immense interest in biomedical applications in the last decades, including theranostics, drug and gene delivery, and vaccine development, owing to their multiple characteristics such as highly defined particle size and shape, amenability to genetic and chemical modifications and encapsulation strategies, as well as good scalability. 1-5 Native plant VNPs exhibit variable immunogenicity and immunostimulatory properties for immunotherapeutic applications (e.g., in situ vaccination for cancer immunotherapy). Many efforts have been made to chemically or genetically modify plants for multiple desired applications. For instance, genetic modification can introduce unnatural amino acids as chemically addressable groups for orthogonal reactions^{3,6} or can create a stabilizer that templates the formation of VNPs, leading to functional protein overcoat⁷ or enzyme encapsulation.8 However, although elegant, these methods require elaborate coding of nucleotides into the viral genome.4 Physical techniques are promising strategies such as encapsulation of small-molecule antitumor drugs⁹ or inorganic NPs¹⁰ into VNPs by the disassembly and reassembly of the viral capsids modulated by electrostatic interactions. However, this approach in turn limits the scope of cargos where negatively charged molecules, macromolecules, or NPs are preferred.¹¹ Another avenue is chemical-based strategies such as bioconjugation methods mediated by mild reactions (*e.g.*, carbodiimide activation and click chemistry) that have emerged as an important approach for virus functionalization.^{12,13} For example, therapeutic drugs, fluorescent dyes, and MRI contrast agents can be loaded onto VNPs *via* a covalent attachment to the reactive amino acid residues on the exterior

Received: November 22, 2021 Accepted: February 28, 2022 Published: March 8, 2022





Scheme 1. Schematic of the Synthesis of MPN Coating on Plant VNPs and Biomedical Applications^a



^aThe phenolic-based coating enables the integration of photoacoustic signals, photothermal transduction, and fluorescent labeling into VNPs (e.g., TMV) through an optional selection of components. In the dashed box, R represents the remainder of the TA molecules, and M^{n+} represents the central metal ions with the oxidation number of n.

or interior surfaces of the viral capsids. 13-16 Nevertheless, these modifications require multiple steps and tedious processing. Therefore, a simple and versatile strategy is of scientific and practical interest to functionalize plant VNPs.

Artificial bioaugmentation has recently attracted immense attention because it can impart functional properties to biomaterials.¹⁷ This strategy involves the exogenous or endogenous coupling of synthetic materials and biological components (e.g., biomacromolecules and living organisms) to afford resulting biohybrids with enhanced performances or new functions. ^{18,19} Metal–organic materials, for example, metal–organic frameworks, ^{20–24} are promising candidates for constructing exogenous functional matrixes or coatings on enzymes, ^{20,24} living cells, ²³ and plant viruses, ^{21,22} and therefore have been widely used for functional biohybrids. Metalphenolic networks (MPNs) are formed via supramolecular interactions (i.e., chelation) between metal ions and natural polyphenols and have gained interest due to their easy synthesis, low toxicity, and high affinity for various biointerfaces.^{25–30} For example, a simple yet dually functional MPN nanoshell was exogenously constructed on individual yeast cells.²⁶ These cells were responsible for external stimuli and were degradable under certain conditions (e.g., pH). We hypothesize that by taking advantage of the adherence of phenolic moieties to a broad choice of functional components, MPN complexes can be easily coated on various plant VNPs, leading to nanohybrids with multifunctional imaging and therapeutic roles.

In this work, we describe a simple and versatile strategy to modify VNPs using MPNs for multiple theranostic purposes including photoacoustic imaging (PAI), photothermal therapy (PTT), and fluorescent labeling (Scheme 1). Specifically, metal ions (e.g., Fe³⁺, Gd³⁺, and Zr⁴⁺) and tannic acid (TA) form MPN coatings with add-on fluorescence (i.e., by embedding fluorescent dyes into the MPN coatings) by

exploiting the adherent nature of phenolic moieties (Figure S1) to various metal ions,³¹ aromatic dyes,³² and proteins.³³ As a proof of concept, we first validated our strategy by using tobacco mosaic virus (TMV)—a rod-shaped nucleoprotein assembly measuring 300 × 18 nm with a 4 nm wide accessible internal channel.³⁴ The proposed multifunctional design fulfills the following purposes: first, by incorporating fluorescent dyes, fluorescent labeling facilitates the direct tracking of TMV via fluorescence microscopy, such as intravital imaging,³⁵ and can serve as a tag for ex vivo quantification, for example, for biodistribution and clearance studies.³⁶ Then, the TMV can afford the PA signal when coated with complexes that induce ligand-to-metal charge-transfer (LMCT) bands (i.e., Fe³⁺-TA). PA imaging is a non-invasive imaging approach that relies on acoustic waves generated by biological tissues or contrast agents upon absorbing light energy; PA imaging allows for a deeper imaging penetration up to \sim 5.2 cm in the NIR-I window (650–950 nm). ^{37–39} Finally, the system offers PTT with minimal invasiveness and precise spatial-temporal control. 40-42 MPN-based materials have been reported to show potentials for PA imaging and PTT.⁴³

Compared to previous strategies on virus modification, our technique has several advantages. First, the synthesis of MPN coatings on VNPs is cost-effective and environmentally friendly, which means it can be finished in a few seconds at room temperature without the need for organic solvents. Second, miscellaneous selection of functional components (*i.e.*, metal ions and fluorescent dyes) provides flexibility for clinical scenarios, such as using Gd³⁺ as a metal ion source for MRI signal enhancement⁴⁺ or near-infrared dyes for imaging-guided therapy. Third, we also demonstrate the robustness of this approach and show that this strategy can be applied to other plant viruses of different shapes, for example, the icosahedral cowpea mosaic virus (CPMV) and the filamentous potato virus X (PVX), which suggests the generalized nature of this

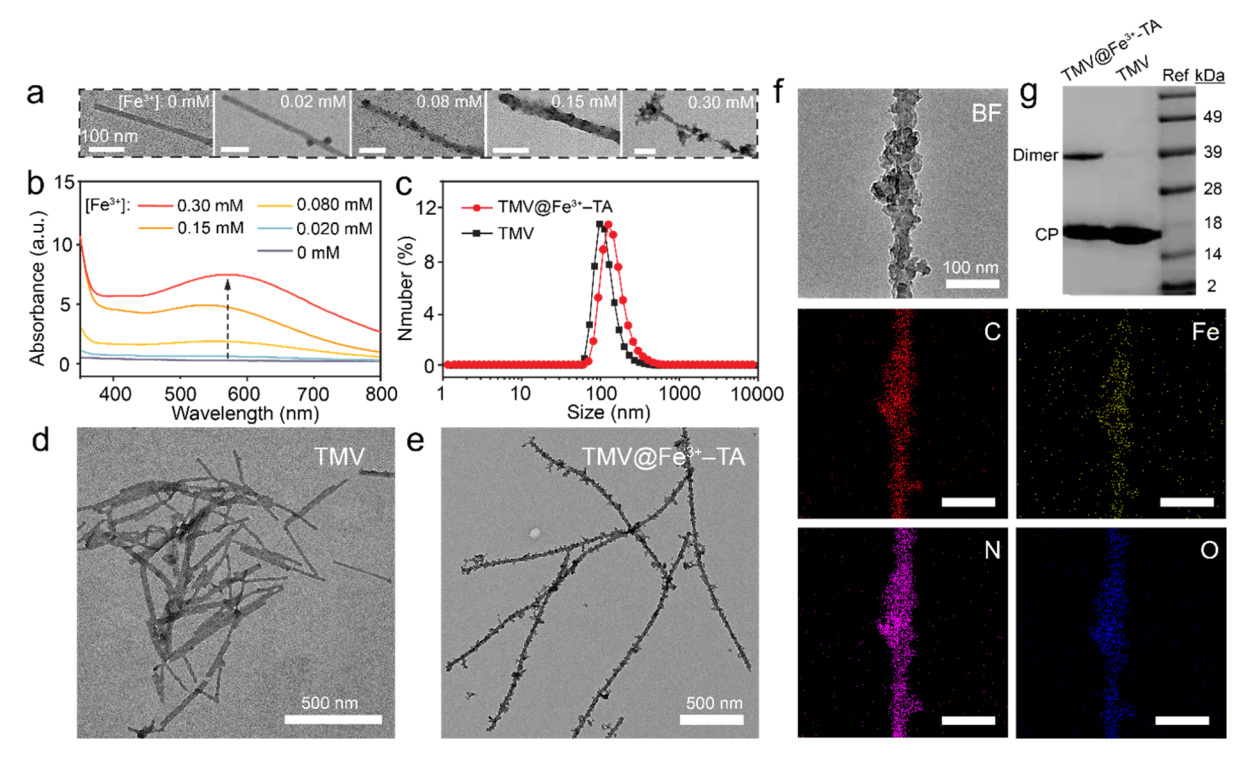


Figure 1. Morphological, spectral, and elemental characterizations of the Fe³+-TA coating on TMV NPs. (a) Illustrative TEM images and (b) UV-vis spectra of TMV@Fe³+-TA with different concentrations of Fe³+ varying from 0 to 0.30 mM (indicated by black arrow). Formulations in (a,b) were labeled by the concentration of Fe³+ only due to the fixed stoichiometry of Fe³+ to TA, which is 3:1. The formulation of Fe³+ (0.15 mM) and TA (0.050 mM) was adopted as the optimized formulation. (c) DLS data showing the size distribution of TMV and TMV@Fe³+-TA. Representative TEM images of (d) bare TMV NPs and (e) TMV@Fe³+-TA nanohybrids. (f) EDX elemental mapping of the TMV@Fe³+-TA nanohybrids. The signal of Fe verified the formation of Fe³+-TA complexes on TMV. (g) SDS-PAGE analysis of the viral capsid protein (CP) from wild-type TMV particles and TMV@Fe³+-TA nanohybrids. CPs from both coated and uncoated TMVs displayed identical electrophoretic profiles, which indicates that their chemical composition remained unchanged after coating. Note that none of the samples were negatively stained. Shared scale bars are 100 nm in (a,f).

method. Relevant studies are compared in Supporting Information (Table S1). We envision that this system will advance VNP-based applications and also facilitate the development of artificial bioaugmentation for a wider range of biomaterials including many protein-based NPs either naturally derived or programmed through origami. 46

2. RESULTS AND DISCUSSION

Plant viruses were propagated in and purified from the leaves of different plant species using established protocols: CPMV particles were extracted from Vigna ungiuculata, and PVX and TMV were isolated from Nicotiana benthamiana.47 The concentrations of purified particles were determined by UV spectrometry at the maximum absorption wavelength of 260 nm for all VNPs (Figure S2a) using the Beer-Lambert law with molar extinction coefficients of 8.1 mL mg⁻¹ cm⁻¹ $(\varepsilon_{\rm CPMV})$, 2.97 mL mg $^{-1}$ cm $^{-1}$ $(\varepsilon_{\rm PVX})$, and 3.0 mL mg $^{-1}$ cm $^{-1}$ $(\varepsilon_{\rm TMV})$. With the UV absorbance of viral RNA peaks at 260 nm and viral coat protein peaks at 280 nm, the ratios between the absorbances at 260 and 280 nm (A_{260}/A_{280}) were found to be 1.78 for CPMV (expected 1.7-1.9), 1.23 for PVX (expected 1.1-1.3), and 1.22 for TMV (expected value of 1.0-1.2), indicating acceptable purity of the produced VNPs. 47 The analysis by size-exclusion fast protein liquid chromatography (FPLC) exhibited a single peak elution profile (Figure S2b). The co-elution of the viral constructs showed the integrity of the prepared particles with negligible broken aggregates. To optimize the coating protocol, we selected TMV particles as a

model VNP; TMV is the most robust platform, and previous data demonstrated the potential of TMV nano-platforms for the development of multifunctional theranostic reagents. 14,16,48-50

The native TMV NPs were coated with MPN (e.g., Fe³⁺-TA) via a one-step method. Specifically, reagents were sequentially added to yield the final concentrations of the TMV suspension (0.22 mg mL $^{-1}$), TA (0.052 mM), Fe $^{3+}$ solution (0.15 mM), and TRIS buffer (10 mM, pH 8.5). The reaction can be finished in seconds. The TMV suspension remained colorless after mixing with TA solution and immediately turned dark blue upon the addition of Fe³⁺ and TRIS buffer due to the formation of Fe³⁺-TA complexes on TMV NPs. The molar ratio of Fe³⁺ and TA was set to 3:1, which is an optimized stoichiometry for the Fe³⁺-TA complex formation via chelation.²⁵ The final concentrations of Fe³⁺ varied from 0 to 0.3 mM, and the optimized formulation was adopted based on the morphology evaluated by transmission electron microscopy (TEM) (Figures 1a and S3), and the coating thickness characterized by UV-vis spectra (Figure 1b). To characterize the morphology, initially, TMV particles with no coating (0 mM Fe³⁺) exhibited a clean and smooth surface. Similarly, the TMV@Fe³⁺-TA (0.02 mM Fe³⁺) displayed no obvious coating on the particle's surface, but there were knotlike structures. At higher concentrations of Fe³⁺ and TA, TMV@Fe³⁺-TA (0.08 mM Fe³⁺) became rougher with dark clumps. In contrast, TMV@Fe³⁺-TA (0.15 mM Fe³⁺) exhibited a smooth and dense coating. When excess precursors

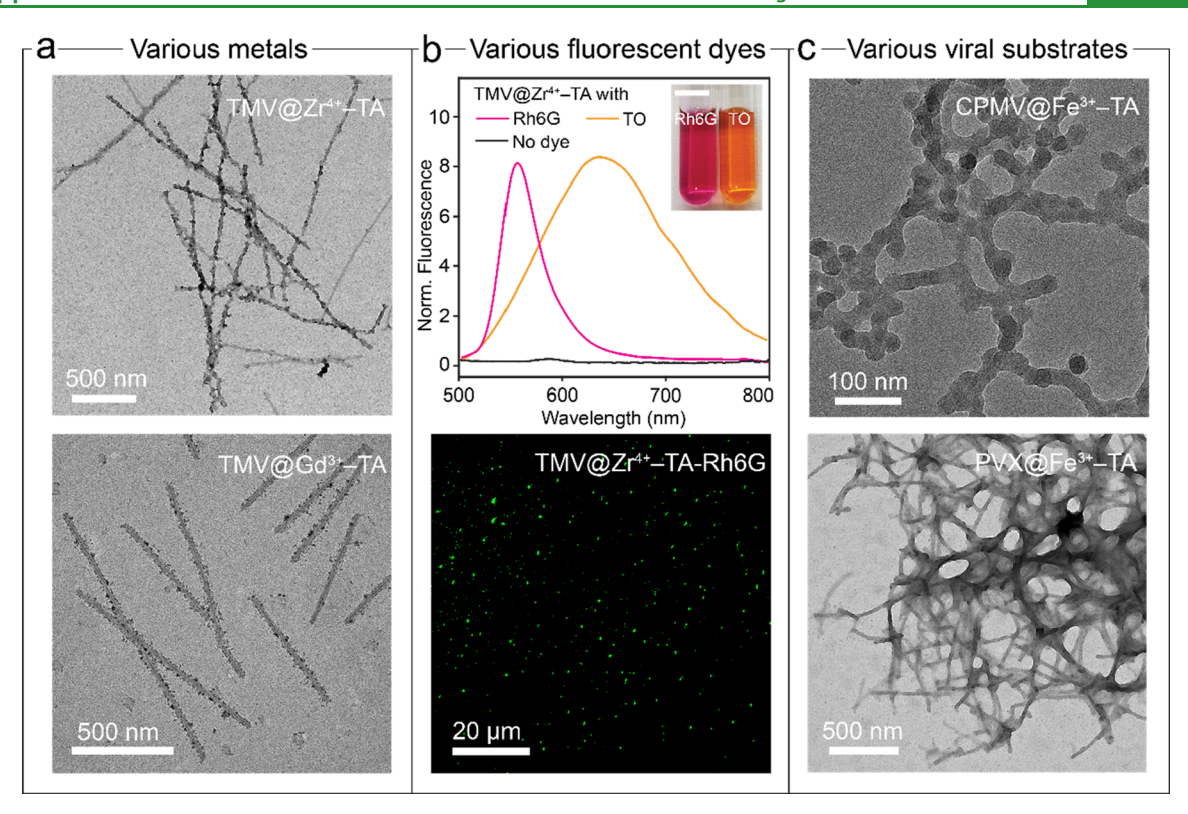


Figure 2. Miscellaneous combination of various metals, fluorescent dyes, and plant VNP substrates for the formation of VNPs@MPN nanohybrids. (a) Option of metals: TEM images of TMV@ Zr^{4+} -TA and TMV@ Gd^{3+} -TA. [Metals] = 0.15 mM; [TA] = 0.050 mM. (b) Option of fluorescent dyes: the upper panel shows normalized fluorescence spectra of suspensions of TMV@ Zr^{4+} -TA loaded with Rh6G and TO. Inset: a photograph of the corresponding suspensions. The lower panel shows TMV@ Zr^{4+} -TA with Rh6G in DI water excited at 488 nm. [Dyes] = 3 μ M; [Zr⁴⁺] = 0.15 mM; [TA] = 0.050 mM. (c) Option of plant VNP substrates: TEM images of icosahedral CPMV@ Fe^{3+} -TA (top panel) and filamentous PVX@ Fe^{3+} -TA (bottom panel). [VNPs] = 0.20mg mL⁻¹; [Fe³⁺] = 0.15 mM; [TA] = 0.050 mM. The scale is 3 mm in the inset of the upper panel in (b).

were added (0.30 mM Fe³⁺), overloaded Fe³⁺—TA complexes were loosely attached to TMV's surface. Increased concentrations of precursors led to TMV@Fe³⁺—TA nanohybrids with a larger absorbance from 350 to 800 nm; the peak was at 570 nm (Figure 1b). The stronger LMCT bands indicate thicker MPN coatings *via* the cross-linking of TA by Fe³⁺ ions. S1 Based on the results from TEM and UV—vis spectra, the formulation of [Fe³⁺]/[TA] = 0.15:0.050 in mM was adopted as the optimized recipe.

Furthermore, to evaluate the optimized TMV@Fe3+-TA nanohybrids, dynamic light scattering (DLS) data showed that the formation of Fe³⁺-TA coating on TMV significantly shifted the surface zeta potential values from -19.2 ± 5.8 to -30.3 ± 11.3 mV [in phosphate-buffered saline (PBS) buffer] and slightly shifted the particle size distribution peak from 99 to 119 nm (Figure 1c), before and after coating, indicating the formation of the coating and absence of noticeable aggregation. Note that although the absolute values of size results from DLS are meant for spherical particles, here they have been used for relative comparison to prove the size change caused by coating and the good dispersion of nanohybrids in water-based buffer. Also, a serial dilution on TMV@Fe³⁺-TA nanohybrids (R^2 = 0.953) also demonstrated their good dispersibility and homogeneity in deionized (DI) water (Figure S4). Furthermore, the TEM images compared the morphology of TMV before and after Fe³⁺-TA coating (Figure 1d,e). Notably, the elongation of coated nanohybrids is attributed to the addition of TA. In an acidic environment, the head-to-tail assembly of TMV is highly favored by minimizing the electrostatic repulsion between the carboxylic residues at the lateral area

of adjunct TMV particles and hydrophobic interactions. 52-54 Energy-dispersive X-ray (EDX) elemental mapping (Figure 1f) and linear scanning (Figure S5) further validated the presence of C, N, and O signals from TMV and TA, as well as Fe signals from the formed Fe³⁺-TA complexes. Sodium dodecyl sulfate-polyacrylamide gel electrophoresis (SDS-PAGE) was used to analyze the TMV coat protein (CP) (Figure 1g). The CP from TMV@Fe3+-TA nanohybrids exhibited a similar electrophoretic profile compared to native uncoated TMV with the expected molecular weight of ~18 kDa,⁵ suggesting that the CP is not covalently modified upon coating with Fe³⁺-TA complexes—as expected. Notably, TMV@Fe3+-TA exhibited an additional band at ~39 kDa corresponding to the CP dimers, which was also previously observed when coating TMV with polydopamine, ^{14,49} perhaps reflecting the intertwining effect of the MPN matrix. ⁴⁸ Overall, the assembly of Fe³⁺– TA complexes on TMV is therefore possibly driven solely by non-covalent intermolecular interactions, such as hydrophobic interactions, hydrogen bonding, and ionic interactions. 33,43,53 In conclusion, we optimized the coating protocol for VNPs@ MPN by selecting TMV and Fe³⁺-TA as models. Nanohybrids with a consistent morphology could be prepared using TMV of $0.20 \text{ mg mL}^{-1} \text{ and } [\tilde{F}e^{3+}]/[TA] = 0.1\hat{5}:0.050 \text{ in mM}, \text{ and we}$ used this formulation for a broader range of nanohybrids and further applications.

Next, to expand the scope of the coating method by using the same formulation optimized above, the modular assembly of VNPs@MPN can be achieved with the miscellaneous selection of functional building blocks, including metal ions (e.g., Gd³+ and Zr⁴+), fluorescent dyes [e.g., rhodamine 6G

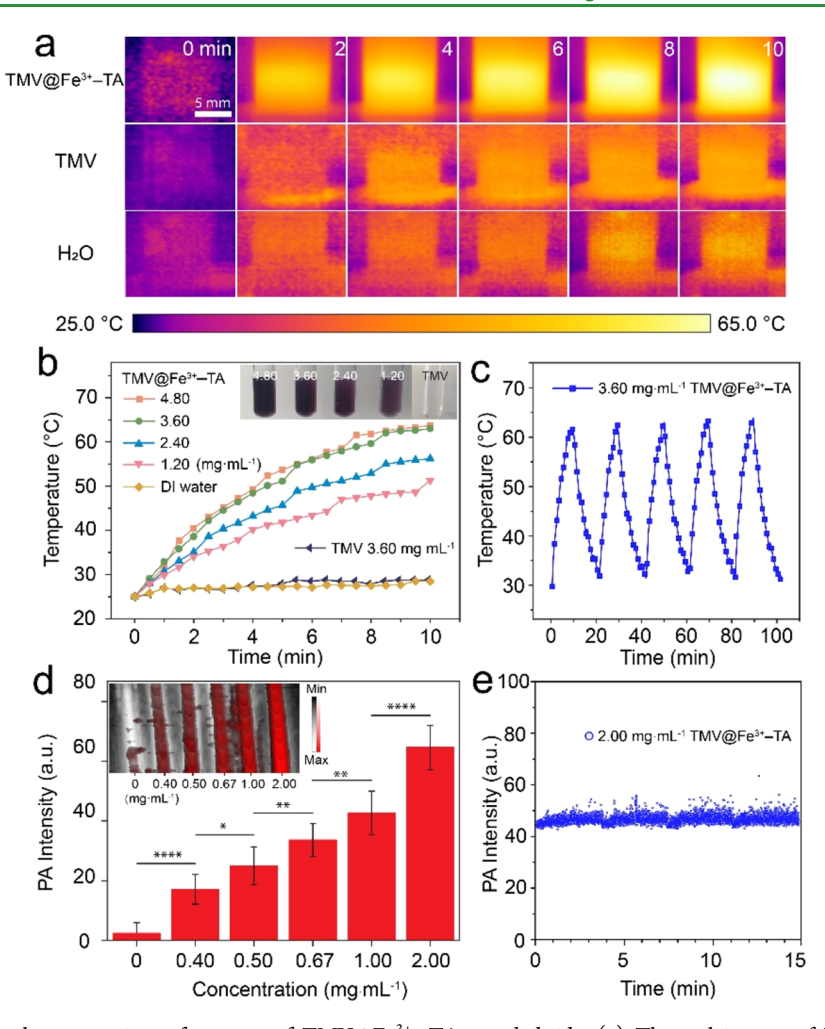


Figure 3. Photothermal and photoacoustic performance of $TMV@Fe^{3+}$ —TA nanohybrids. (a) Thermal images of $TMV@Fe^{3+}$ —TA (3.60 mg mL⁻¹), pure TMV (3.60 mg mL⁻¹), and DI water upon 808 nm irradiation for 10 min. (b) Temperature profiles of $TMV@Fe^{3+}$ —TA suspensions irradiated by an 808 nm laser (1.0 W cm⁻²). Inset: a photograph of $TMV@Fe^{3+}$ —TA at different concentrations (from left to right: 4.80, 3.60, 2.40, and 1.20 mg mL⁻¹ $TMV@Fe^{3+}$ —TA, and 2.00 mg mL⁻¹ pure TMV). (c) Photothermal stability of $TMV@Fe^{3+}$ —TA (3.60 mg mL⁻¹) with an 808 nm laser. The sample experienced five cycles of heating and cooling. (d) PA intensity of $TMV@Fe^{3+}$ —TA in elevated concentrations when illuminated by a 680 nm laser (n = 9 regions of interest). Inset: dual PA—US image of the samples. The data were processed using ImageJ. Signals in red and white represent PA and ultrasound (US), respectively. (e) Time-dependent photostability test of $TMV@Fe^{3+}$ —TA (2.00 mg mL⁻¹) for 15 min.

(Rh6G) and thiazole orange (TO)] (Figure S1), and different plant VNP substrates (e.g., PVX and CPMV). 31,32,43 First, various metals coordinate with TA via chelation, and the physicochemistry of the resulting complexes is largely dependent on the type of metal ion and the corresponding oxidation number.³¹ For example, the Fe³⁺-based MPN was welldemonstrated to be highly biocompatible; 26 tetra-valent metal ions (e.g., Zr⁴⁺) were generally more stable and thicker than di- or tri-coordinating ions; and Gd3+ ions can afford the MPN with MRI signals in clinical diagnosis. 44 Representative TEM images showed TMV nanohybrids enabled by MPN with Zr⁴⁺ and Gd³⁺(Figure 2a). UV-vis spectra demonstrated increased absorbance in the range of 300-380 nm for particles coated with increasing concentrations of Zr⁴⁺ and Gd³⁺ (Figure S6). DLS results (Figure S7) showed that the sizes of TMV@ Zr⁴⁺-TA particles were larger than those of TMV@Fe³⁺-TA and TMV@Gd3+-TA particles, which can be explained by the higher coordination numbers of Zr4+. Furthermore, various aromatic fluorescent dyes interact with TA by $\pi - \pi$ stacking and cation- π interactions. This inspired us to investigate the incorporation of fluorescent dyes (i.e., Rh6G and TO) into

the biohybrids. The Zr4+-based MPN was chosen for fluorescent labeling due to its relatively lower extinction compared to the Fe³⁺-TA coating (Figure S8). The fluorescence spectra showed that the TMV@Zr4+-TA nanohybrids were loaded with Rh6G or TO; fluorescence microscopy confirmed green fluorescence from TMV@Zr4+-TA-Rh6G excited at 488 nm (Figure 2b). To estimate the fluorescence performance of such TMV@Zr4+-TA-Rh6G nanohybrids, linear regression ($R^2 = 0.995$) was plotted; the fluorescence intensity is roughly equivalent to 0.49 µM of free Rh6G solution in DI water when 3.0 μ M of Rh6G was used to synthesize such nanohybrids (Figure S9). The loss of fluorescent intensity was also observed when loading rhodamine B on polystyrene, reflecting the quenching effect of TA.³² The fluorescent MPN complexes with various dyes have been proven to be stable on polystyrene at a pH ranging from 1 to 8 and in complex biological media incubating for 24 h, which is attributed to dominant π interactions between the dyes and phenolic motifs.³²

Finally, we investigated the coating on VNPs of different shapes, that is, PVX and CPMV. PVX is an elongated,

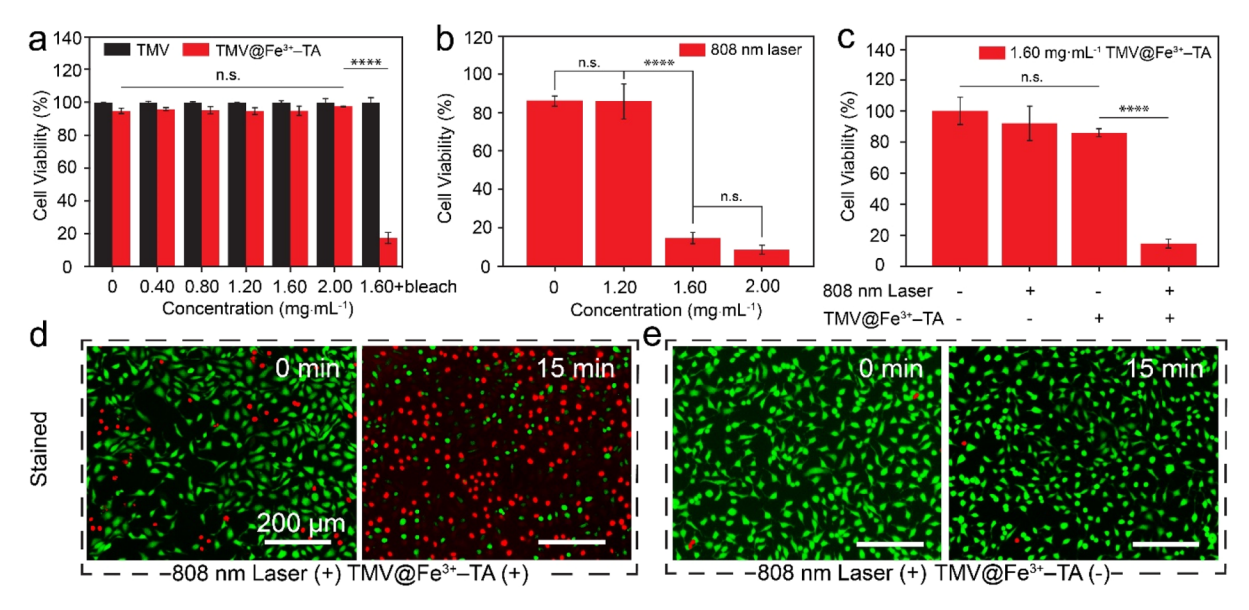


Figure 4. Cell cytotoxicity and thermal ablation performance on SKOV3 using TMV@Fe³+-TA nanohybrids. (a) Cell viability of SKOV3 cells determined with the resazurin toxicology assay after incubating with different concentrations of TMV and TMV@Fe³+-TA for 24 h. (b) Concentration-dependent cell viability after photothermal treatment (808 nm laser, 1.0 W cm⁻² for 15 min) following a 24 h incubation with different concentrations of TMV@Fe³+-TA (0-2.0 mg mL⁻¹). (c) Comparative cell viability for different treatment regimens: 808 nm laser on (+) or off (-) for 15 min, combined with (+) or without (-) the incubation of 1.60 mg mL⁻¹ of TMV@Fe³+-TA for 24 h. The experiments in a-c were conducted in triplicate. Fluorescence images of SKOV3 with (d) combination of laser irradiation (808 nm, 15 min) and TMV@Fe³+-TA (1.60 mg mL⁻¹) incubation for 24 h and (e) laser irradiation only. Staining: calcein AM and PI. Significant difference: ****p < 0.0001 and n.s. = no significant difference (p > 0.05).

filamentous, and flexible VNP that has a high aspect ratio (515 × 13 nm), while CPMV is an icosahedral virus with a diameter of 30 nm. Using the same coating formulation that produces TMV@Fe³⁺-TA (i.e., 0.15 mM Fe³⁺, 0.15 mM TA, and 0.20 mM VNPs), successful designs of PVX@Fe³⁺-TA and CPMV@Fe³⁺-TA were confirmed by TEM (Figure 2c). In addition, DLS data showed that the formation of Fe³⁺-TA coating on CPMV and PVX resulted in increased particle sizes when compared to the native VNPs (Figure S10 and Table S3). The values of surface zeta potentials were more negative (Table S2). Side-by-side TEM images of all coated and uncoated viruses showed distinct coatings that are in high contrast (Figure S11). These observations indicate that Fe³⁺-TA coatings were successfully formed on different VNPs. SDS-PAGE was used to analyze the CPs from uncoated VNPs (i.e., CPMV and PVX) and VNPs@Fe3+-TA. Irrespective of the type of VNPs, the CPs of the coated VNPs described similar electrophoretic profiles compared to the uncoated CPs (Figure \$12). This is consistent with the results obtained for TMV and indicates no breakage of protein and unchanged chemical compositions due to the mild reaction conditions and the noncovalent nature of MPN, as described in Figure 1g. Collectively, we demonstrated miscellaneous combinations available for the formation of VNPs@MPN nanohybrids.

Among a different selection of components for practical applications, the strong extinction of LMCT of Fe³⁺-TA implies photo-mediated applications such as PTT performance and PA imaging.⁴⁵ The color of Fe³⁺-TA complexes is bluish-black because the complexes strongly absorb light in the visible and NIR-I regions.⁵⁵ This motivated us to investigate the photothermal conversion capability imparted by the Fe³⁺-TA coating. The temperature profiles of TMV@Fe³⁺-TA (3.60 mg mL⁻¹), TMV (3.60 mg mL⁻¹), and DI water irradiated with an 808 nm laser were monitored using a near-infrared

(NIR) camera (Figure 3a). Specifically, the heating profiles and maximum temperature were used to evaluate thermal performance, while the cooling profiles were used to calculate the photothermal conversion efficiency (η) . Calculation and example data can be found in the Supporting Information. First, when irradiated by an 808 nm laser, concentrationdependent (TMV@ Fe^{3+} -TA nanohybrids = 0, 1.20, 2.40, 3.60, and 4.80 mg mL⁻¹) temperature profiles show a quicker temperature rise and higher maximum temperatures as the concentrations increase. The temperature profile of the pure TMV suspension (3.60 mg mL⁻¹) was similar to that of DI water, while the maximum temperature for the TMV@Fe³⁺-TA suspension (63.6 °C) was significantly higher than the pure TMV's (3.3 °C). Furthermore, power-dependent temperature profiles show the maximum temperature of TMV@Fe3+-TA nanohybrids (3.60 mg mL⁻¹) increased from 37.0 to 82.8 °C as the laser power increased from 0.33 to 1.5 W cm⁻² (Figure S13). Finally, the η was averaged to be 33.2% based on three independent measurements under different power densities of 0.33, 0.50, and 1.00 W cm⁻², $R^2 = 0.99$ (Figure S14 and Table S4). The value of η is close to that of pure Fe³⁺-TA and Fe³⁺-EGCG complexes and higher than that of phenolic-based nanohybrids, such as Gd3+-DOTA-TMV@PDA and PVP@ Fe³⁺-TA (summarized in Table S5). 14,56,57 The thermal stability test showed that the photothermal performance of TMV@Fe3+-TA remained unchanged after five circles of irradiation (Figure 3c). Likewise, the TEM images showed that supramolecular coatings had no obvious exfoliation after repeated irradiation (Figure S15), suggesting that the TMV@Fe3+-TA nanohybrids are promising photothermal agents for PTT.

We further assessed the PA performance because the PA and photothermal properties are always correlated. 44 TMV@Fe $^{3+}$ TA (2.00 mg mL $^{-1}$) exhibited clear PA signals from 680 to 900

nm (Figure S16); the highest signal was at 680 nm. In contrast, native TMV at the same concentrations (2.00 mg mL⁻¹) showed negligible PA signal enhancement (data not shown), indicating that the Fe³⁺-TA coating is responsible for the PA signals displayed by the TMV@ Fe³⁺-TA. We selected the 680 nm laser as the light source and studied the concentration-dependent PA performance. Specifically, the PA signals of TMV@Fe³⁺-TA exhibited a good linear relationship ($R^2 = 0.94$) from 0 to 2.00 mg mL⁻¹ (Figures 3d and S17). Based on the previous method, ^{58,59} the limit of detection (LOD) of PA was determined to be 17.7 μ g mL⁻¹ in DI water (Figure S18). Moreover, we observed a negligible PA intensity drop in the continuous irradiation of the 680 nm laser for 15 min (Figure 3e), which indicated its potential for prolonged PA imaging.⁶⁰

We finally evaluated the cytotoxicity of the TMV@Fe³⁺-TA and tested their photothermal cancer cell-killing capabilities. The in vitro cell viability was conducted using human ovarian adenocarcinoma SKOV3 cells. After an incubation of 24 h, both TMV and TMV@Fe3+-TA of up to 2.00 mg mL-1 did not show obvious cytotoxicity (Figure 4a). Laser irradiation (808 nm laser, 1.0 W cm⁻² for 15 min) was applied on the SKOV3 cells incubated with different concentrations of TMV@ Fe^{3+} -TA (i.e., 0, 0.40, 0.80, 1.20, 1.60, and 2.00 mg mL⁻¹). Cells were incubated at 1.60 mg mL⁻¹ and treated by thermal bleaching (58 °C, 15 min) as a positive control. Cell viability decreased from 86 to 13% when the concentrations of TMV@Fe³⁺-TA increased from 1.20 to 1.60 mg mL⁻¹ (Figure 4b). Therefore, the concentration of 1.60 mg mL⁻¹ was selected to evaluate the thermal ablation efficacy. Compared to the cell viability of groups treated only with the laser (92%) or only with TMV@Fe³⁺-TA (85%), the cell viability of the group treated with both the laser and TMV@Fe3+-TA decreased to 15% (Figure 4c). A fluorescence-based live/ dead cell assay was further used to visualize the cytocompatibility and thermal ablation performance of TMV@Fe³⁺-TA at 1.60 mg mL⁻¹ (Figures 4d,e and S19). All cells were stained with calcein AM and propidium iodide (PI) dyes simultaneously to identify live cells (green fluorescence) and dead cells (red fluorescence). Fluorescent images demonstrate that significant cell death was caused by the combination of laser irradiation and TMV@Fe3+-TA incubation, which is consistent with the data from the cell viability assessment (Figure 4c).

3. CONCLUSIONS

We described a one-step and versatile approach for multifunctional coating on viral NPs via MPNs. We demonstrated the miscellaneous combination of functional components (e.g., metal ions, dyes, and VNPs) to form a coating that imparts multifunction to viral NPs, including combined imaging modalities (e.g., fluorescent labeling and PAI) and therapeutic effects (e.g., PTT). The cell-killing capacity was demonstrated to be effective. Since the obtained biohybrids were biocompatible and fully encapsulated, this strategy might also be used to protect virus-based vaccines from storage failure, especially in those developing regions where constant refrigeration is not always available. The multifunctional and biocompatible coating strategy will underpin a promising platform for proteinaceous therapeutics, virus-based recombinant vaccines, biosensing, catalysts, and more potential applications.

4. EXPERIMENTAL SECTION

- **4.1. Materials.** TA, iron(III) chloride hexahydrate (FeCl₃·6H₂O, 97%), gadolinium(III) chloride hexahydrate (GdCl₃·6H₂O, 99%), zirconyl chloride octahydrate (ZrOCl₂·8H₂O, 98%), Rh6G, and TO were purchased from Sigma-Aldrich. 2-amino-2-(hydroxymethyl)-1,3-propanediol (TRIS, >98%) was purchased from Tokyo Chemical Industry Co., Ltd. (TCI). Organic solvents including *N,N*-dimethylformamide (sequencing grade) and dimethyl sulfoxide (certified ACS) were obtained from Fisher Scientific International, Inc. (Hampton, NH). PI (\geq 95%) was purchased from Combi-Blocks (San Diego, CA, USA). Resazurin and McCoy's 5A medium were purchased from Sigma-Aldrich (Atlanta, GA, USA). TEM grids (200 mesh) were obtained from Ted Pella, Inc. High-purity water with a resistivity of 18.2 M Ω cm was obtained from an inline Millipore RiOs/Origin water purification system. All solutions were freshly prepared for immediate use in each experiment.
- **4.2. Plant Virus NP Preparation.** Plant viruses were propagated in and purified from the leaves of different plant species following established protocols.⁴⁷ CPMV particles were extracted from *V. ungiuculata*; PVX and TMV were isolated from the same plant species *N. benthamiana*. The concentration of TMV was measured on a NanoDrop 2000 spectrophotometer (Thermo Fisher Scientific).
- **4.3. Characterization.** The integrity of plant virus nanoparticles (VNPs) was analyzed by size-exclusion FPLC on an ÄKTA Explorer chromatography system equipped with a Superose 6 column (GE Healthcare). TEM images were acquired using a JEOL JEM 1400 Plus operating at 80 kV with a Gatan 4k digital camera. Electron-dispersive X-ray spectroscopy (EDS) images were performed using Thermo Fisher Talos 200X operating at 200 kV. Scanning TEM images and EDS mapping were performed by using Thermo Scientific software. DLS measurements were performed on a Malvern Nano-ZS90 Zetasizer to acquire hydrodynamic sizes and zeta-potential values of the viral NPs and biohybrids. UV-visible absorption measurements were performed on a BioTek Synergy H1 microplate reader. The ratio of A_{260} to A_{280} values was acquired using the Thermo Scientific NanoDrop One^C spectrophotometer. Temperature profiles and contours were recorded with an FLIR Cx-Series compact thermal imaging camera. Photoacoustic (PA) images and signals were collected using VisualSonics Vevo 2100-LAZR. PA signals were processed using ImageJ software.6
- 4.4. Encapsulation of Plant VNPs with MPNs. All solutions were freshly prepared for immediate use. The standard preparation process is described as follows: in a 2 mL tube, 100 μ L of VNP dispersion (2 mg mL⁻¹) was first added dropwise to 660 μ L of DI water with a vigorous vortex. Next, 20 µL of TA solution (4 mg mL⁻¹) was added dropwise while gently vortexing, followed by a onetime addition of 40 μ L of the fresh metal solution (Fe³⁺ of 0.95 mg mL⁻¹ as an example). The dispersion was then vigorously vortexed to yield the final concentrations (metal: 0.15 mM of FeCl₃·6H₂O, ZrOCl₂·8H₂O, and GdCl₃·6H₂O; TA: 0.050 mM; plant VNPs: 0.20 mg mL-1 of TMV, CPMV, and PVX). The pH was then raised to \sim 8.0 by adding 80 μ L of TRIS buffer (10 mM, pH 8.5). The resulting particles were then washed with DI water three times to remove excess metal-TA complexes, and the particles were pelleted by centrifugation (20,000g, 10 min). The supernatant was then completely removed, and pellets were redispersed in DI water to obtain a VNPs@MPN biohybrid for further characterization. All syntheses were conducted under an ambient atmosphere and at room temperature.
- **4.5.** Sodium Dodecyl Sulfate-Polyacrylamide Gel Electrophoresis. A mixture of VNP samples with the loading buffer (made of 62.5 mM Tris-HCl pH 6.8, 2% (w/v) SDS, 10% (v/v) glycerol, 0.01% (w/v) bromophenol blue, and 10% (v/v) 2-mercaptoethanol) was boiled at 100 °C for 5 min. The resultant samples were loaded on 12% NuPAGE polyacrylamide gels run in 1× [3-(N-morpholino)-propane sulfonic acid]buffer (MOPS, Invitrogen) for 40 min at 200 V.⁴⁷ SeeBlue Plus2 pre-stained protein standards (Thermo Fisher Scientific) were used to provide the weight ladder markers. Following

the run, the gels were stained with Coomassie brilliant blue and imaged on the AlphaImager system (Protein Simple).

- 4.6. Dye Attachment for Fluorescent Labeling. TA and fluorescent dyes were added into the TMV dispersion with vigorous vortex followed by the addition of ZrOCl₂·8H₂O solution to yield the following final concentrations (dyes: 3.0 µM of thiazole orange or rhodamine 6G; ZrOCl₂·8H₂O: 0.15 mM; TMV: 0.20 mg mL⁻¹; and TA: 0.050 mM). The pH was adjusted to ~8.0 by TRIS buffer (80 mL, 10 mM, pH 8.5), and the system was reacted for 30 min. The resulting particles were then washed with DI water three times to remove the excess complex in the supernatant; the particles were centrifuged (20,000g, 10 min), the supernatant was completely removed, and the pellets were redispersed in DI water to obtain fluorescent TMV particles. The resulting particles were characterized using a plate reader or by fluorescent microscopy.
- 4.7. PAI of TMV@Fe³⁺-TA. A VisualSonics Vevo 2100 LAZR imaging system was used to take the PA signal. Samples were imaged using a 21 MHz-centered LZ 250 transducer, and the peak energy is 45 ± 5 mJ at 20 Hz at the source. The laser was calibrated and optimized before the sample measurement. The specimens were positioned at a depth of 1 cm from the transducer. The PA intensity spectra were obtained in the range of 680-900 nm. The PA and ultrasonic images of the samples were taken at 808 nm. All PA data were processed using ImageJ software. The average value and standard deviation (SD) of the PA intensity were calibrated based on the nine regions of interest per tube.
- 4.8. Cell Culture and Preparation. Human ovarian adenocarcinoma (SKOV3) cells were cultured in McCoy's 5A medium (1.5 mM L-glutamine and 2.2 g L⁻¹ sodium bicarbonate supplemented with 10% fetal bovine serum and 1% penicillin-streptomycin). Cells are cultured under 5% CO₂ at 37 °C. Cultures were given at least three passages before they were used for experiments. Cells were passaged to 75-80% confluency using 0.25% trypsin-EDTA.
- 4.9. Cell Staining with Calcein AM and PI Dyes. SKOV3 cells were seeded in a 24-well plate (50,000 cells per well) for 24 h, incubated with TMV@Fe³⁺—TA at a final concentration of 1.60 mg mL⁻¹ for 24 h, irradiated by an 808 nm laser for 15 min, and were incubated for 24 h. Afterward, 1000 μ L of mixture solution of calcein AM (2 μ M, live staining) and PI (6 μ M, dead staining) was added, and the cells were incubated for 30 min to stain the SKOV3 cells. After washing with PBS, the fluorescence images of each sample were captured using the EVOS FL fluorescence microscope in GFP and RGP channels.
- 4.10. In Vitro PTT at 808 nm Irradiation. SKOV3 cells were divided in a 96-well plate at a concentration of 10,000 cells/well and seeded for 24 h to allow the cells to attach to the plate. The medium was then replaced with a mixture of the medium and TMV@Fe³⁺-TA dispersion at a final concentration of 1.60 mg mL⁻¹ and cultured for 24 h. The experimental wells were exposed to an 808 nm laser with a power density of 1.0 W cm⁻¹ for 15 min. After incubation for 24 h, the wells were washed three times with PBS to remove the free TMV@Fe³⁺-TA particles. Resazurin dye solution equal to 10% of the culture medium volume was added to stain the cells; the cells were incubated for 3 h, and the cell viability was measured fluorometrically by monitoring the increase in fluorescence at an emission wavelength of 590 nm using an excitation wavelength of 560 nm. A complete medium without cells was used as a blank for a viable quantitative calculation. All cell experiments were conducted in triplicate.
- **4.11. Cytotoxicity Assay.** Cells were prepared and stained using the same method as that described above. The concentrations of samples are 0, 0.20, 0.40, 0.80, 1.20, 1.60, and 2.00 mg mL⁻¹. Cells with pure TMV particles at the same concentrations were used as control experiments. A complete medium without cells was used as a blank for viability quantitation.
- 4.12. Statistical Analysis. Cell experiments were conducted in triplicate. The average value and SD of the PA intensity were calibrated based on the nine regions of interest per tube. All statistical analyses were processed using Origin 2018 or ImageJ software. All data were represented as the average ± SD. Error bars represent the SD of the mean. Statistical analysis: a p-value less than 0.05 was

statistically significant [*p < 0.05, **p < 0.01, ***p < 0.001, ****p < 0.001, ***p < 0.001, **p < 00.0001, n.s. = no significant difference (p > 0.05)].

4.13. Calculation of Photothermal Conversion Efficiency. The photothermal conversion efficiency (η) of the TMV@Fe³⁺-TA nanohybrids was determined according to the previous method. 62 The detailed calculation was given as follows

$$\sum_{i} m_{i} C_{p,i} \frac{\mathrm{d}T}{\mathrm{d}t} = Q_{\mathrm{NP}} + Q_{\mathrm{sys}} - Q_{\mathrm{diss}}$$
 (1)

where m and C_p are the mass (1.0 g) and specific heat capacity [4.18 J $(g\ ^{\circ}C)^{-1}]$ of the system components, respectively. Q_{NP} is the energy input of the TMV@Fe3+-TA NPs, Q_{sys} expresses the energy input of the container (i.e., quartz cuvette) with the solvent (i.e., DI water), and Q_{diss} represents the energy dissipation from the cuvette and the solvent in the form of heat.

The term of energy input of TMV@Fe3+-TA NPs, QNP, can be expressed as follows

$$Q_{NP} = I(1 - 10^{-A_{\lambda}})\eta \tag{2}$$

where I is the laser power in watt, A_{λ} is the absorbance of NPs at the wavelength of the laser, and η is the photothermal conversion

The term of energy dissipation from the system can be expressed

$$Q_{\rm diss} = hS(T - T_{\rm surr}) \tag{3}$$

where h is the heat transfer coefficient, S is the surface area of the container, and T_{surr} is the temperature of the surroundings.

When the temperature reaches an equilibrium (T_{max}) , dT/dt = 0. Therefore, eq 1 becomes

$$0 = Q_{NP} + Q_{sys} - Q_{diss}$$
 (4)

At this stage, the energy dissipation equals the total energy input terms, $Q_{NP} + Q_{sys}$

$$Q_{NP} + Q_{sys} = Q_{diss} = hS(T_{max} - T_{surr})$$
(5)

In the next experimental stage, the laser is turned off to allow energy dissipation only. Therefore, the terms of $Q_{\rm NP}$ and $Q_{\rm sys}$ become zero, and eq 1 becomes

$$\sum_{i} m_{i} C_{p,i} \frac{\mathrm{d}T}{\mathrm{d}t} = -Q_{\text{diss}} = -hS(T - T_{\text{surr}})$$
(6)

Rearranging eq 6 gives

$$dt = -\frac{\sum_{i} m_{i} C_{p,i}}{hS} \frac{dT}{T - T_{surr}}$$
(7)

Integration of eq 7 gives

$$t = -\frac{\sum_{i} m_{i} C_{p,i}}{hS} \ln \frac{T - T_{\text{surr}}}{T_{\text{max}} - T_{\text{surr}}}$$
(8)

To determine the energy dissipation term, hS, the system time constant τ_s is introduced

$$\tau_{\rm s} = \frac{\sum_{i} m_{i} C_{p,i}}{hS} \tag{9}$$

and a dimensionless parameter theta is defined as

$$\theta = \frac{T - T_{\text{surr}}}{T_{\text{max}} - T_{\text{surr}}} \tag{10}$$

Substituting eqs 9 and 10 into eq 8 gives

$$t = -\tau_{\rm s} \ln \theta \tag{11}$$

By using eq 11, the time constant τ_s can be determined by plotting the linear regression of t in seconds versus the negative natural logarithm of θ plotted as shown in Figure S14. Recording starts (t = 0) at the time when the laser is turned off and the temperature drops. $Q_{\rm diss}$ can be determined independently by calculating hS' from the cuvette and the solvent in the absence of NPs

$$Q_{diss} = hS'(T_{max,H_2O} - T_{surr})$$
(12)

The photothermal conversion efficiency can be determined by the equation

$$\eta = \frac{hS(T_{\text{max}} - T_{\text{surr}}) - Q_{\text{diss}}}{I(1 - 10^{-A_{\lambda}})}$$
(13)

4.14. Calculation of LOD. The LOD of the TMV@Fe³⁺-TA nanohybrids was determined according to the previous method. ^{58,59} The detailed calculation was given as follows. The LOD was determined using the limit of blank (LOB). The LOB is defined as the highest signal generated from a sample that contains no analyte. It is calculated by taking a replicate of a blank sample and finding the mean and SD.

$$LOB = mean_{blank} + 1.645(SD_{blank})$$
 (14)

The LOB encompasses 95% of the observed blank values, while the remaining 5% contains a response that could have been generated from a low analyte concentration. The LOD is defined as the minimum analyte concentration that can be reliably distinguished from the LOB.

$$LOD = LOB + 1.645(SD_{low concentration})$$
 (15)

The LOD represents an analyte concentration in which 95% of the measured samples are distinguishable from the LOB, while the remaining 5% erroneously appear to contain no analyte. In our experiments, the LOB and LOD were calculated from Figure S18 using values of PA intensity when the concentrations of nanohybrids were 0 and 400 μ g mL⁻¹, respectively.

ASSOCIATED CONTENT

Solution Supporting Information

The Supporting Information is available free of charge at https://pubs.acs.org/doi/10.1021/acsami.1c22690.

Materials, instrumentations, characterization, methods, measurement and calculation of photothermal conversion efficiency, and LOD (PDF)

AUTHOR INFORMATION

Corresponding Authors

Nicole F. Steinmetz – Department of NanoEngineering, Department of Bioengineering, Moores Cancer Center, and Center for NanoImmunoEngineering, Department of Radiology, Center for Nano-ImmunoEngineering, and Institute for Materials Discovery and Design, University of California San Diego, La Jolla, California 92093, United States; orcid.org/0000-0002-0130-0481; Email: nsteinmetz@ucsd.edu

Jesse V. Jokerst — Department of NanoEngineering, Materials Science and Engineering Program, and Department of Radiology, University of California San Diego, La Jolla, California 92093, United States; ⊚ orcid.org/0000-0003-2829-6408; Email: jjokerst@ucsd.edu

Authors

Zhuohong Wu − Department of NanoEngineering, University of California San Diego, La Jolla, California 92093, United States; occid.org/0000-0002-5318-9092

- Jiajing Zhou Department of NanoEngineering, University of California San Diego, La Jolla, California 92093, United States; orcid.org/0000-0001-5203-4737
- Christian Isalomboto Nkanga Department of NanoEngineering, University of California San Diego, La Jolla, California 92093, United States
- Zhicheng Jin Department of NanoEngineering, University of California San Diego, La Jolla, California 92093, United States; orcid.org/0000-0001-6072-7533
- Tengyu He Materials Science and Engineering Program, University of California San Diego, La Jolla, California 92093, United States; Occid.org/0000-0002-6767-4849
- Raina M. Borum Department of NanoEngineering, University of California San Diego, La Jolla, California 92093, United States; oorcid.org/0000-0003-4265-3109
- Wonjun Yim Materials Science and Engineering Program, University of California San Diego, La Jolla, California 92093, United States; oorcid.org/0000-0002-0242-7898
- Jingcheng Zhou Department of NanoEngineering, University of California San Diego, La Jolla, California 92093, United States
- Yong Cheng Department of NanoEngineering, University of California San Diego, La Jolla, California 92093, United States
- Ming Xu Department of NanoEngineering, University of California San Diego, La Jolla, California 92093, United States; orcid.org/0000-0002-6998-8462

Complete contact information is available at: https://pubs.acs.org/10.1021/acsami.1c22690

Author Contributions

Z.W., J.Z., and C.I.N. contributed equally to this work. N.F.S. and J.V.J. are co-corresponding authors.

Notes

The authors declare the following competing financial interest(s): Dr. Steinmetz is a co-founder of and has a financial interest in Mosaic ImmunoEngineering, Inc. The other authors do not declare a conflict of interest.

■ ACKNOWLEDGMENTS

Dr. Uli Commandeur (RWTH Aachen University) is thanked for providing PVX. J.V.J. acknowledges NIH funding under S10 OD021821, R21 AG065776, and the NSF grant 1845683. N.F.S. acknowledges NIH grant R01 CA202814. R.M.B. acknowledges fellowship support under T32 CA153915. This work was performed in part at the San Diego Nanotechnology Infrastructure (SDNI) of University of California, San Diego, a member of the National Nanotechnology Coordinated Infrastructure (NNCI), which is supported by the National Science Foundation (Grant ECCS-1542148). The electron microscopic images were taken in the Cellular and Molecular Medicine Electron microscopy core facility, which is supported in part by the National Institutes of Health Award number S10OD023527. The fluorescent images were taken at the UC San Diego School of Medicine Microscopy Core, which is supported by NINDS P30 core grant (NS047101). This work was partially supported by NSF through the UC San Diego Materials Research Science and Engineering Center (UCSD MRSEC), DMR-2011924. Graphics were created with Biorender.com.

REFERENCES

- (1) Lizotte, P. H.; Wen, A. M.; Sheen, M. R.; Fields, J.; Rojanasopondist, P.; Steinmetz, N. F.; Fiering, S. In Situ Vaccination with Cowpea Mosaic Virus Nanoparticles Suppresses Metastatic Cancer. *Nat. Nanotechnol.* **2016**, *11*, 295–303.
- (2) Steele, J. F. C.; Peyret, H.; Saunders, K.; Castells-Graells, R.; Marsian, J.; Meshcheriakova, Y.; Lomonossoff, G. P. Synthetic Plant Virology for Nanobiotechnology and Nanomedicine. *Wiley Interdiscip. Rev.: Nanomed. Nanobiotechnol.* **2017**, *9*, No. e1447.
- (3) Chung, Y. H.; Cai, H.; Steinmetz, N. F. Viral Nanoparticles for Drug Delivery, Imaging, Immunotherapy, and Theranostic Applications. *Adv. Drug Delivery Rev.* **2020**, *156*, 214–235.
- (4) Shahgolzari, M.; Pazhouhandeh, M.; Milani, M.; Yari Khosroushahi, A.; Fiering, S. Plant Viral Nanoparticles for Packaging and In Vivo Delivery of Bioactive Cargos. *Wiley Interdiscip. Rev.: Nanomed. Nanobiotechnol.* **2020**, *12*, No. e1629.
- (5) Nkanga, C. I.; Steinmetz, N. F. The Pharmacology of Plant Virus Nanoparticles. *Virology* **2021**, *556*, 39–61.
- (6) Hovlid, M. L.; Lau, J. L.; Breitenkamp, K.; Higginson, C. J.; Laufer, B.; Manchester, M.; Finn, M. G. Encapsidated Atom-Transfer Radical Polymerization in Qbeta Virus-Like Nanoparticles. *ACS Nano* **2014**, *8*, 8003–8014.
- (7) Sharma, J.; Uchida, M.; Miettinen, H. M.; Douglas, T. Modular Interior Loading and Exterior Decoration of a Virus-Like Particle. *Nanoscale* **2017**, *9*, 10420–10430.
- (8) Fiedler, J. D.; Brown, S. D.; Lau, J. L.; Finn, M. G. RNA-Directed Packaging of Enzymes within Virus-Like Particles. *Angew. Chem., Int. Ed.* **2010**, *49*, 9648–9651.
- (9) Cai, H.; Shukla, S.; Steinmetz, N. F. The Antitumor Efficacy of CpG Oligonucleotides is Improved by Encapsulation in Plant Virus-Like Particles. *Adv. Funct. Mater.* **2020**, *30*, 1908743.
- (10) Li, L.; Xu, C.; Zhang, W.; Secundo, F.; Li, C.; Zhang, Z.-P.; Zhang, X.-E.; Li, F. Cargo-Compatible Encapsulation in Virus-Based Nanoparticles. *Nano Lett* **2019**, *19*, 2700–2706.
- (11) Mieloch, A. A.; Kręcisz, M.; Rybka, J. D.; Strugała, A.; Krupiński, M.; Urbanowicz, A.; Kozak, M.; Skalski, B.; Figlerowicz, M.; Giersig, M. The Influence of Ligand Charge and Length on the Assembly of Brome mosaic Virus Derived Virus-Like Particles with Magnetic Core. *AIP Adv.* **2018**, *8*, 035005.
- (12) Chen, Z.; Li, N.; Li, S.; Dharmarwardana, M.; Schlimme, A.; Gassensmith, J. J. Viral Chemistry: the Chemical Functionalization of Viral Architectures to Create New Technology. Wiley Interdiscip. Rev.: Nanomed. Nanobiotechnol. 2016, 8, 512–534.
- (13) Mohan, K.; Weiss, G. A. Chemically Modifying Viruses for Diverse Applications. ACS Chem. Biol. 2016, 11, 1167–1179.
- (14) Hu, H.; Yang, Q.; Baroni, S.; Yang, H.; Aime, S.; Steinmetz, N. F. Polydopamine-Decorated Tobacco Mosaic Virus for Photoacoustic/Magnetic Resonance Bimodal Imaging and Photothermal Cancer Therapy. *Nanoscale* **2019**, *11*, 9760–9768.
- (15) Schlick, T. L.; Ding, Z.; Kovacs, E. W.; Francis, M. B. Dual-Surface Modification of the Tobacco Mosaic Virus. *J. Am. Chem. Soc.* **2005**, *127*, 3718–3723.
- (16) Bruckman, M. A.; Jiang, K.; Simpson, E. J.; Randolph, L. N.; Luyt, L. G.; Yu, X.; Steinmetz, N. F. Dual-Modal Magnetic Resonance and Fluorescence Imaging of Atherosclerotic Plaques In Vivo Using VCAM-1 Targeted Tobacco Mosaic Virus. *Nano Lett.* **2014**, *14*, 1551–1558.
- (17) Cao, J.; Zaremba, O. T.; Lei, Q.; Ploetz, E.; Wuttke, S.; Zhu, W. Artificial Bioaugmentation of Biomacromolecules and Living Organisms for Biomedical Applications. *ACS Nano* **2021**, *15*, 3900–3926.
- (18) Guo, Z.; Richardson, J. J.; Kong, B.; Liang, K. Materials Approaches for Bioaugmentation. *Sci. Adv.* **2020**, *6*, No. eaaz0330.
- (19) Zeng, Z.; Pu, K. Improving Cancer Immunotherapy by Cell Membrane-Camouflaged Nanoparticles. *Adv. Funct. Mater.* **2020**, *30*, 2004397.
- (20) Liang, K.; Ricco, R.; Doherty, C. M.; Styles, M. J.; Bell, S.; Kirby, N.; Mudie, S.; Haylock, D.; Hill, A. J.; Doonan, C. J.; Falcaro, P. Biomimetic Mineralization of Metal—organic Frameworks as

- Protective Coatings for Biomacromolecules. Nat. Commun. 2015, 6, 7240.
- (21) Li, S.; Dharmarwardana, M.; Welch, R. P.; Ren, Y.; Thompson, C. M.; Smaldone, R. A.; Gassensmith, J. J. Template-Directed Synthesis of Porous and Protective Core-Shell Bionanoparticles. *Angew. Chem., Int. Ed.* **2016**, *55*, 10691–10696.
- (22) Luzuriaga, M. A.; Welch, R. P.; Dharmarwardana, M.; Benjamin, C. E.; Li, S.; Shahrivarkevishahi, A.; Popal, S.; Tuong, L. H.; Creswell, C. T.; Gassensmith, J. J. Enhanced Stability and Controlled Delivery of MOF-Encapsulated Vaccines and their Immunogenic Response In Vivo. ACS Appl. Mater. Interfaces 2019, 11, 9740–9746.
- (23) Liang, K.; Richardson, J. J.; Cui, J.; Caruso, F.; Doonan, C. J.; Falcaro, P. Metal—organic Framework Coatings as Cytoprotective Exoskeletons for Living Cells. *Adv. Mater.* **2016**, *28*, 7910–7914.
- (24) Lian, X.; Erazo-Oliveras, A.; Pellois, J.-P.; Zhou, H.-C. High Efficiency and Long-Term Intracellular Activity of an Enzymatic Nanofactory Based on Metal—Organic Frameworks. *Nat. Commun.* **2017**, *8*, 2075.
- (25) Ejima, H.; Richardson, J. J.; Liang, K.; Best, J. P.; van Koeverden, M. P.; Such, G. K.; Cui, J.; Caruso, F. One-Step Assembly of Coordination Complexes for Versatile Film and Particle Engineering. *Science* **2013**, *341*, 154–157.
- (26) Park, J. H.; Kim, K.; Lee, J.; Choi, J. Y.; Hong, D.; Yang, S. H.; Caruso, F.; Lee, Y.; Choi, I. S. A Cytoprotective and Degradable Metal—Polyphenol Nanoshell for Single-Cell Encapsulation. *Angew. Chem., Int. Ed.* **2014**, *126*, 12628—12633.
- (27) Zhang, Z.; Xie, L.; Ju, Y.; Dai, Y. Recent Advances in Metal—Phenolic Networks for Cancer Theranostics. *Small* **2021**, *17*, No. e2100314.
- (28) Zhou, J.; Lin, Z.; Penna, M.; Pan, S.; Ju, Y.; Li, S.; Han, Y.; Chen, J.; Lin, G.; Richardson, J. J.; Yarovsky, I.; Caruso, F. Particle Engineering Enabled by Polyphenol-Mediated Supramolecular Networks. *Nat. Commun.* **2020**, *11*, 4804.
- (29) Jokerst, J.; Zhou, J.; Xu, M.; Jin, Z.; Borum, R.; Avakyan, N.; Cheng, Y.; Yim, W.; He, T.; Zhou, J.; Wu, Z.; Mantri, Y. Versatile Polymer Nanocapsules via Redox Competition. *Angew. Chem., Int. Ed.* **2021**, *60*, 26357–26362.
- (30) Jin, Z.; Mantri, Y.; Retout, M.; Cheng, Y.; Zhou, J.; Jorns, A.; Fajtova, P.; Yim, W.; Moore, C.; Xu, M.; Creyer, M.; Borum, R.; Zhou, J.; Wu, Z.; He, T.; Penny, W.; O'Donoghue, A.; Jokerst, J. A Charge-Switchable Zwitterionic Peptide for Rapid Detection of SARS-CoV-2 Main Protease. *Angew. Chem., Int. Ed.* **2022**, *61*, No. e202112995.
- (31) Guo, J.; Ping, Y.; Ejima, H.; Alt, K.; Meissner, M.; Richardson, J. J.; Yan, Y.; Peter, K.; von Elverfeldt, D.; Hagemeyer, C. E.; Caruso, F. Engineering Multifunctional Capsules through the Assembly of Metal—Phenolic Networks. *Angew. Chem., Int. Ed.* **2014**, *53*, 5546—5551.
- (32) Lin, Z.; Zhou, J.; Qu, Y.; Pan, S.; Han, Y.; Lafleur, R. P. M.; Chen, J.; Cortez-Jugo, C.; Richardson, J. J.; Caruso, F. Luminescent Metal—Phenolic Networks for Multicolor Particle Labeling. *Angew. Chem., Int. Ed.* **2021**, *60*, 24968–24975.
- (33) Han, Y.; Lin, Z.; Zhou, J.; Yun, G.; Guo, R.; Richardson, J. J.; Caruso, F. Polyphenol-Mediated Assembly of Proteins for Engineering Functional Materials. *Angew. Chem., Int. Ed.* **2020**, *59*, 15618–15625.
- (34) Lomonossoff, G. P.; Wege, C. TMV Particles: The Journey From Fundamental Studies to Bionanotechnology Applications. *Adv. Virus Res.* **2018**, *102*, 149–176.
- (35) Lewis, J. D.; Destito, G.; Zijlstra, A.; Gonzalez, M. J.; Quigley, J. P.; Manchester, M.; Stuhlmann, H. Viral Nanoparticles as Tools for Intravital Vascular Imaging. *Nat. Med.* **2006**, *12*, 354–360.
- (36) Robertson, K. L.; Liu, J. L. Engineered Viral Nanoparticles for Flow Cytometry and Fluorescence Microscopy Applications. *Wiley Interdiscip. Rev.: Nanomed. Nanobiotechnol.* **2012**, *4*, 511–524.
- (37) Wang, L. V.; Hu, S. Photoacoustic Tomography: In Vivo Imaging from Organelles to Organs. *Science* **2012**, *335*, 1458–1462.

- (38) Miao, Q.; Pu, K. Organic Semiconducting Agents for Deep-Tissue Molecular Imaging: Second Near-Infrared Fluorescence, Self-Luminescence, and Photoacoustics. *Adv. Mater.* **2018**, *30*, 1801778.
- (39) Zhou, J.; Jokerst, J. V. Photoacoustic Imaging with Fiber Optic Technology: A Review. *Photoacoustics* **2020**, *20*, 100211.
- (40) Lee, D.-E.; Koo, H.; Sun, I.-C.; Ryu, J. H.; Kim, K.; Kwon, I. C. Multifunctional Nanoparticles for Multimodal Imaging and Theragnosis. *Chem. Soc. Rev.* **2012**, *41*, 2656–2672.
- (41) Zhen, X.; Cheng, P.; Pu, K. Recent Advances in Cell Membrane-Camouflaged Nanoparticles for Cancer Phototherapy. *Small* **2019**, *15*, No. e1804105.
- (42) Li, J.; Zhen, X.; Lyu, Y.; Jiang, Y.; Huang, J.; Pu, K. Cell Membrane Coated Semiconducting Polymer Nanoparticles for Enhanced Multimodal Cancer Phototheranostics. *ACS Nano* **2018**, 12, 8520–8530.
- (43) Wu, D.; Zhou, J.; Creyer, M. N.; Yim, W.; Chen, Z.; Messersmith, P. B.; Jokerst, J. V. Phenolic-Enabled Nanotechnology: Versatile Particle Engineering for Biomedicine. *Chem. Soc. Rev.* **2021**, *50*, 4432–4483.
- (44) Park, S.-m.; Aalipour, A.; Vermesh, O.; Yu, J. H.; Gambhir, S. S. Towards Clinically Translatable In Vivo Nanodiagnostics. *Nat. Rev. Mater.* **2017**, *2*, 17014.
- (45) Liu, Y.; Bhattarai, P.; Dai, Z.; Chen, X. Photothermal Therapy and Photoacoustic Imaging via Nanotheranostics in Fighting Cancer. *Chem. Soc. Rev.* **2019**, *48*, 2053–2108.
- (46) Bhaskar, S.; Lim, S. Engineering Protein Nanocages as Carriers for Biomedical Applications. *NPG Asia Mater* **2017**, *9*, No. e371.
- (47) Wen, A. M.; Lee, K. L.; Yildiz, I.; Bruckman, M. A.; Shukla, S.; Steinmetz, N. F. Viral Nanoparticles for In Vivo Tumor Imaging. *J. Visualized Exp.* **2012**, *69*, No. e4352.
- (48) Hu, H.; Zhang, Y.; Shukla, S.; Gu, Y.; Yu, X.; Steinmetz, N. F. Dysprosium-Modified Tobacco Mosaic Virus Nanoparticles for Ultra-High-Field Magnetic Resonance and Near-Infrared Fluorescence Imaging of Prostate Cancer. ACS Nano 2017, 11, 9249–9258.
- (49) Nkanga, C. I.; Chung, Y. H.; Shukla, S.; Zhou, J.; Jokerst, J. V.; Steinmetz, N. F. The In Vivo Fate of Tobacco Mosaic Virus Nanoparticle Theranostic Agents Modified by the Addition of a Polydopamine Coat. *Biomater. Sci.* **2021**, *9*, 7134–7150.
- (50) Liu, X.; Wu, F.; Tian, Y.; Wu, M.; Zhou, Q.; Jiang, S.; Niu, Z. Size Dependent Cellular Uptake of Rod-Like Bionanoparticles with Different Aspect Ratios. *Sci. Rep.* **2016**, *6*, 24567.
- (51) Rahim, M. A.; Ejima, H.; Cho, K. L.; Kempe, K.; Müllner, M.; Best, J. P.; Caruso, F. Coordination-Driven Multistep Assembly of Metal—Polyphenol Films and Capsules. *Chem. Mater.* **2014**, *26*, 1645–1653.
- (52) Niu, Z.; Bruckman, M.; Kotakadi, V. S.; He, J.; Emrick, T.; Russell, T. P.; Yang, L.; Wang, Q. Study and Characterization of Tobacco Mosaic Virus Head-to-Tail Assembly Assisted by Aniline Polymerization. *Chem. Commun.* **2006**, 28, 3019–3021.
- (53) Chariou, P. L.; Ma, Y.; Hensley, M.; Rosskopf, E. N.; Hong, J. C.; Charudattan, R.; Steinmetz, N. F. Inactivated Plant Viruses as an Agrochemical Delivery Platform. *ACS Agric. Sci. Technol.* **2021**, *1*, 124–130.
- (54) Stubbs, G. Tobacco Mosaic Virus Particle Structure and the Initiation of Disassembly. *Philos. Trans. R. Soc., B* **1999**, 354, 551–557.
- (55) Liu, F.; He, X.; Chen, H.; Zhang, J.; Zhang, H.; Wang, Z. Gram-Scale Synthesis of Coordination Polymer Nanodots with Renal Clearance Properties for Cancer Theranostic Applications. *Nat. Commun.* **2015**, *6*, 8003.
- (56) Wang, Y.; Liu, F.; Yan, N.; Sheng, S.; Xu, C.; Tian, H.; Chen, X. Exploration of Fe(III)—Phenol Complexes for Photothermal Therapy and Photoacoustic Imaging. *ACS Biomater. Sci. Eng.* **2019**, *5*, 4700—4707.
- (57) Zhao, G.; Wu, H.; Feng, R.; Wang, D.; Xu, P.; Jiang, P.; Yang, K.; Wang, H.; Guo, Z.; Chen, Q. Novel Metal Polyphenol Framework for MR Imaging-Guided Photothermal Therapy. ACS Appl. Mater. Interfaces 2018, 10, 3295–3304.

- (58) Armbruster, D. A.; Pry, T. Limit of blank, Limit of Detection and Limit of Quantitation. *Clin. Biochem. Rev.* **2008**, 29, S49–S52.
- (59) Creyer, M. N.; Jin, Z.; Moore, C.; Yim, W.; Zhou, J.; Jokerst, J. V. Modulation of Gold Nanorod Growth via the Proteolysis of Dithiol Peptides for Enzymatic Biomarker Detection. *ACS Appl. Mater. Interfaces* **2021**, *13*, 45236–45243.
- (60) Yim, W.; Zhou, J.; Mantri, Y.; Creyer, M. N.; Moore, C. A.; Jokerst, J. V. Gold Nanorod–Melanin Hybrids for Enhanced and Prolonged Photoacoustic Imaging in the Near-Infrared-II Window. ACS Appl. Mater. Interfaces 2021, 13, 14974–14984.
- (61) Schindelin, J.; Arganda-Carreras, I.; Frise, E.; Kaynig, V.; Longair, M.; Pietzsch, T.; Preibisch, S.; Rueden, C.; Saalfeld, S.; Schmid, B.; Tinevez, J.-Y.; White, D. J.; Hartenstein, V.; Eliceiri, K.; Tomancak, P.; Cardona, A. Fiji: An Open-Source Platform for Biological-Image Analysis. *Nat. Methods* **2012**, *9*, 676–682.
- (62) Zhou, J.; Jiang, Y.; Hou, S.; Upputuri, P. K.; Wu, D.; Li, J.; Wang, P.; Zhen, X.; Pramanik, M.; Pu, K.; Duan, H. Compact Plasmonic Blackbody for Cancer Theranosis in the Near-Infrared II Window. ACS Nano 2018, 12, 2643–2651.

